Novelty Journals

ISSN 2394-9678

International Journal of Novel Research in Electrical and Mechanical Engineering
Vol. 5, Issue 1, pp: (19-29), Month: September 2017 - August 2018, Available at: www.noveltyjournals.com

Use of Panel Method in High Subsonic and Transonic Aerodynamic Analysis of Complex Aircraft Configuration

Ahmed Tawfeeq Mustafa Abed

Baghdad, Iraq

Abstract: **The application of low order panel method with the Dirichlet boundary condition on complex aircraft configuration have been studied in high subsonic and transonic speeds. Low order panel method has been used to solve the case of the steady, inviscid and compressible flow on a forward swept wing – canard configuration with cylindrical fuselage and a vertical stabilizer with symmetrical cross section. The aerodynamic coefficients for the forward swept wing aircraft were calculated using measured wake shape from an experimental work on same model configuration. The study showed that the application of low order panel method can be used with acceptable results.**

Keywords: **Panel Method, Numerical aerodynamic analysis, Computational fluid dynamic, Forward Swept Wing, Aerodynamic Characteristics, Wing-Canard Configuration.**

I. INTRODUCTION

The idea behind sweeping the wings is to reduce the compressibility effect. As shown in Fig. (1) the chordwise component of the flow will be decoupled into two components reducing the Mach number locally. The same can be obtained regardless of the sweep direction but an inboard flow will result in the case of forward sweep. Outward flow of the aft sweep results in tip stalls first, as the stall progresses the control surfaces will lose effectiveness due to flow separation over these surfaces. Root separated first in forward swept wing allowing the control surfaces to maintain its effectiveness to a higher angle of attack. Other feature of forward sweeping is the span loading form that is nearly elliptical; this will result in a smaller vortex drag than aft sweep. The higher angle of attack range with the smaller drag offered by the forward sweep means higher maneuverability.

Introducing a canard can enhance the performance of the forward swept wing by delaying the root separation to a higher angle of attack, as the downwash of the canard decreases the local angle of attack at the wing part covered by the canard flow field. This will result in reduction in the drag, too. Another advantage is the use of the canard as a control surface (horizontal stabilizer) instead of or in conjunction with the horizontal tail. Placing the horizontal stabilizer in the undisturbed flow increases its effectiveness through a higher range of flight conditions. The canard can play this role, as it is located in front of the wing away from any flow disturbance.

Novelty Journals

ISSN 2394-9678

International Journal of Novel Research in Electrical and Mechanical Engineering
Vol. 5, Issue 1, pp: (19-29), Month: September 2017 - August 2018, Available at: www.noveltyjournals.com

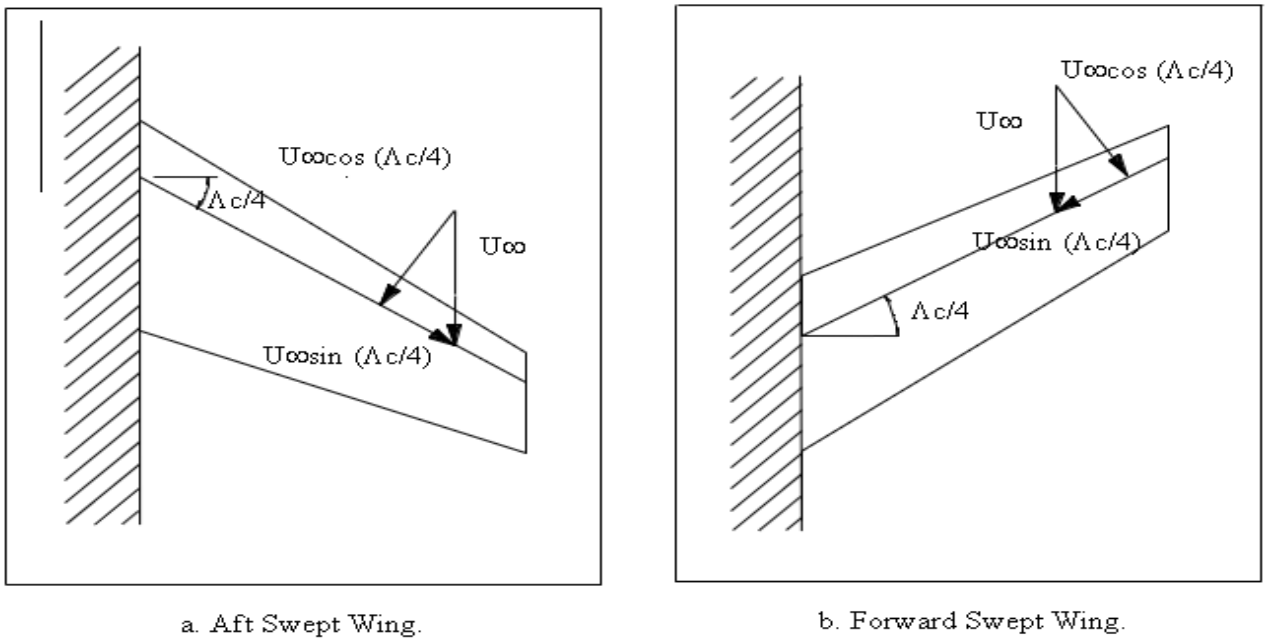

Fig. (1) Velocity Components on ASW and FSW

II. LITERATURE REVIEW

Michael J. Mann and Charles E. Mercer (1986), investigated the design of a FSW fighter configuration and an assessment has been made of the relative performance of forward vs. aft sweep. A model of this configuration was tested in a transonic tunnel. The results show that if the FSW were designed with a canard a chordwise pressure distribution could be developed at transonic maneuver conditions which would produce less flow separation than that resulting for a wing without a canard. The FSW configuration showed good maneuver performance at Mach (0.6,0.9 and 1.2) relative to HiMAT fighter configuration. At Mach (0.9) and lift coefficient higher than (0.9) the FSW had lower drag than that of the HiMAT due to the favorable influence of the canard.

Whipple, Raymonnd and others (1986), made an experimental test for a (1/8) model of the X-29 aircraft at (0.2) Mach number. The angle of attack ranged from (40°) to (90°) and the angle of sideslip ranged from (-10°) to (30°). Data were obtained for the basic design and for several forebody strakes.

John W. Hicks and Thomas Huckabone (1989), made a complete in flight tests to determine the subsonic lift and drag characteristics of the X-29A airplane. They found that these values met, or exceeded predictions, particularly with respect to the drag polar shapes. Induced drag levels were as low as 20 percent less than wind tunnel estimates. Drag polar shape comparisons with other modern fighter aircraft showed the X-29A to have a better overall aircraft aerodynamic Oswald efficiency factor (e) for the same aspect ratio.

Edwin J. Saltzman and John W. Hicks (1994), obtained the in flight lift and drag characteristics of the X-29A airplane for Mach numbers from (0.4) to (1.3). The X-29A data were compared with three high performance fighter aircraft's, the F-15C, F-16C and F/A –18. The lifting efficiency of the X-29A (e) is about average for a cantilevered monoplane for (M = 0.6) and angles of attack up to those required for maximum L/D ratio. At (M = 0.6) the levels of L/D and (e), as a function of load factor for the X-29A was about the same as for the contemporary aircraft.

Arnott A. D. and Berstin L. (2000), made an analysis for the aerodynamic interference at the FSW and plate interaction region with a fully developed turbulent boundary layer. Flow visualization and surface pressure distribution have been made for a model at Reynolds number (1.03×10^6) based on the wing chord and free stream velocity equal (30 m/s). For low stall angles, boundary layer separation was wake at the plate while at higher angles many separation regions have been noticed with a large three-dimensional vortex region.

Novelty Journals

ISSN 2394-9678

International Journal of Novel Research in Electrical and Mechanical Engineering
Vol. 5, Issue 1, pp: (19-29), Month: September 2017 - August 2018, Available at: www.noveltyjournals.com

III. MATHEMATICAL MODEL

The method described in Katz (1991) will be used in the present work. The continuity equation for the case of the steady state, incompressible, irrotational flow in terms of the total potential (Φ) is:

$$\nabla^2\Phi = 0 \tag{1}$$

The general solution to Eq. (1) can be constructed by a sum of source (σ) and doublet (μ) distribution placed on the boundary (S) shown in Fig. (2):

$$\Phi = \frac{1}{4\pi}\int_S \left[\mu\vec{n}\cdot\nabla\left(\frac{1}{r}\right) - \sigma\left(\frac{1}{r}\right)\right]dS + \Phi_\infty \tag{2}$$

Where ($\vec{n}$) is the normal vector on the surface (S) and in the direction of the potential jump (μ) and (Φ_∞) is the free stream potential:

$$\Phi_\infty = U_\infty x + V_\infty y + W_\infty z \tag{3}$$

For enclosed boundary the potential inside the body is constant which may be selected to yield different panel method techniques. If this constant is set to (Φ_∞) then Eq. 2 will be:

$$\frac{1}{4\pi}\int_{body+wake} \mu\vec{n}\cdot\nabla\left(\frac{1}{r}\right)dS - \frac{1}{4\pi}\int_{body} \sigma\left(\frac{1}{r}\right)dS = 0 \tag{4}$$

Using the Dirichlet boundary condition, the source strength can be set to:

$$\sigma = Q_\infty\cdot\vec{n} \tag{5}$$

The solution can be constructed from doublet element only and by setting the constant value of the inner potential to (0) then Eq. (2) will reduced to:

$$\frac{1}{4\pi}\int_{body+wake} \mu\vec{n}\cdot\nabla\left(\frac{1}{r}\right)dS + \Phi_\infty = 0 \tag{6}$$

The wake doublet distribution is related to the unknown doublets on (S) by using the Kutta condition along the trailing edge:

$$\mu_W = \mu_u - \mu_l \tag{7}$$

The body in Fig. (2) is now divided into (NB) surface panels and (NW) wake panels as shown in Fig. (3). The Dirichlet boundary condition will be specified at each body panel at a "collocation point". Eq. (4) is applied for each of the (N_B) collocation points resulting:

$$\sum_{k=1}^{N_B}\frac{1}{4\pi}\int_{body} \mu\vec{n}\cdot\nabla\left(\frac{1}{r}\right)dS + \sum_{l=1}^{N_W}\frac{1}{4\pi}\int_{wake} \mu\vec{n}\cdot\nabla\left(\frac{1}{r}\right)dS - \sum_{k=1}^{N_B}\frac{1}{4\pi}\int_{body} \sigma\left(\frac{1}{r}\right)dS = 0 \tag{8}$$

The integration is limited now to each individual panel and for a unit singularity element (σ or μ) it depends on the panel geometry only. For a constant-strength (μ) element the influence of panel (k) at any point (P) is:

$$\frac{1}{4\pi}\int_{1,2,3,4} \frac{\partial}{\partial\vec{n}}\left(\frac{1}{r}\right)dS_k \equiv C_k$$

And for a constant-strength (σ) element:

$$-\frac{1}{4\pi}\int_{1,2,3,4}\left(\frac{1}{r}\right)dS_k \equiv B_k$$

After computing the influence of each panel on each other panel, Eq. (8) will be:

$$\sum_{k=1}^{N_B} C_k\mu_k + \sum_{l=1}^{N_W} C_l\mu_l + \sum_{k=1}^{N_B} B_k\sigma_k = 0 \qquad (9)$$

Using Eq. (5) the coefficients (B_k) can be calculated and can be moved to the right hand side of the equation. The wake doublet (μ_w) is related to the upper and lower trailing edge doublet (μ_u) and (μ_l) by Eq. (7). Then the influence of the wake element becomes:

$$C_W\mu_W = C_W(\mu_u - \mu_l) \qquad (10)$$

Consequently, for each collocation point (P), a linear algebraic equation containing (N_B) unknown singularity variables (μ_k) can be derived:

$$\sum_{k=1}^{N_B} A_k\mu_k = -\sum_{k=1}^{N_B} B_k\sigma_k \qquad (11)$$

Where $A_k = C_k \mp C_w$ for Trailing edge panels

$A_k = C_k$ for other panels

Evaluating Eq. (11) at each of the (N_B) collocation points results in (N_B) equations with (N_B) unknown (μ_k), or:

$$[A]\{\mu\} = -[B]\{\sigma\} \qquad (12)$$

If Eq. (6) is used we can get a similar result but the right hand side will be the free stream potential:

$$[A]\{\mu\} = \{\Phi_\infty\} \qquad (13)$$

These equations represent a system of linear algebraic equations that can be solved using numerical solvers. Once Eq. (12) or Eq. (13) is solved the unknown singularity values are obtained and the velocity components can be evaluated in terms of the panel local coordinates as follows:

$$u = \frac{\partial\mu}{\partial l} \qquad (14a)$$

$$v = \frac{\partial\mu}{\partial m} \qquad (14b)$$

where (l) and (m) are the two tangential components of the local coordinate system.

The total velocity (Q_k) in the local direction of panel (k) is obtained by adding the free stream velocity components in the local coordinates to the perturbation velocity. The pressure coefficient can be computed at each panel using Bernoulli equation:

$$C_{Pk} = 1 - Q_k^2 / Q_\infty^2 \qquad (15)$$

The horizontal and normal components of the total aerodynamic forces are calculated from:

$$F_x = 0.5\rho Q_\infty^2 \sum_{k=1}^{N_B} C_{Pk} A_k n_{xk} \quad (16a)$$

$$F_z = 0.5\rho Q_\infty^2 \sum_{k=1}^{N_B} C_{Pk} A_k n_{zk} \quad (16b)$$

Where

A_k = area of each body panel

n_{xk} and n_{zk} = components of each unit normal vector ($\vec{n}$) in the global x-axis and z-axis directions.

The lift and drag coefficients are calculated from:

$$C_L = \frac{F_z \cos\alpha - F_x \sin\alpha}{0.5\rho Q_\infty^2 S_{ref}} \quad (17a)$$

$$C_D = \frac{F_z \sin\alpha + F_x \cos\alpha}{0.5\rho Q_\infty^2 S_{ref}} \quad (17b)$$

Where S_{ref} is the plane form area (surface area) and (α) is the angle of attack.

The pitching moment (M_P) around the leading edge induced by the aerodynamic forces at any collocation points is calculated from:

$$M_P = 0.5\rho Q_\infty^2 \left[\sum_{k=1}^{N_B} \left(C_P A n_x\right)_k Z_{ck} + \left(C_P A n_z\right)_k X_{ck} \right] \quad (18)$$

Where (X_{ck}, Z_{ck}) are global coordinates of each collocation point. The pitching moment coefficient is:

$$C_M = \frac{M_P}{0.5\rho Q_\infty^2 S_{ref} C_{ref}} \quad (19)$$

Where (C_{ref}) any reference length (such as the chord length) that the pitching moment is calculated with respect to.

The Prandtl-Glauert rule is used to incorporate the effects of "low speed compressibility". For the case when the free stream flow is parallel to the (x) coordinate then that coordinate is being stretched with increased Mach number, while the (y) and (z) coordinates remain unchanged.

$$\beta^2 \Phi_{xx} + \Phi_{yy} + \Phi_{zz} = 0 \quad (20)$$

Where

$$\beta^2 = 1 - M^2 \quad (21)$$

Once the (x) coordinate is transformed, the equivalent incompressible potential problem is solved and the aerodynamic coefficients must be transformed back to the compressible case by dividing them by (β).

Novelty Journals

ISSN 2394-9678

International Journal of Novel Research in Electrical and Mechanical Engineering
Vol. 5, Issue 1, pp: (19-29), Month: September 2017 - August 2018, Available at: www.noveltyjournals.com

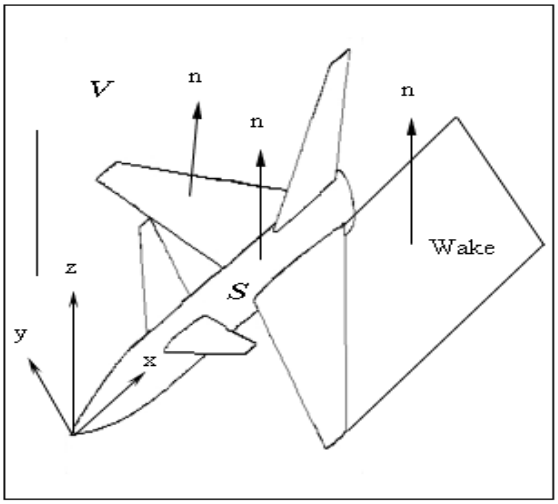

Fig. (2) Potential Flow Over Closed Body.

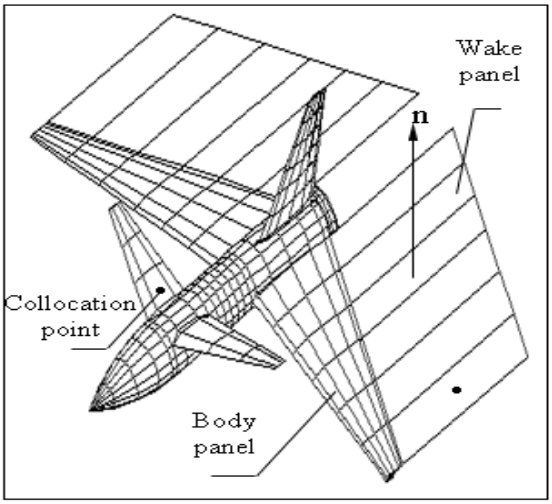

Fig. (3) Discretization of the Body using Flat Panels.

IV. THE FORWARD SWEPT WING CONFIGURATION

The numerical method presented will be used to calculate the aerodynamic coefficients of the FSW model shown in Fig. (4) for configuration (1) and (2). The wing and the canard wakes are modeled using a measured wakes shape from experimental work on the same model. It is assumed that the wake geometry is not changed with the change of the free stream Mach number. The full body discretization is shown in Fig. (5) with total number of panels (elements) equals to (1714) for half of the body.

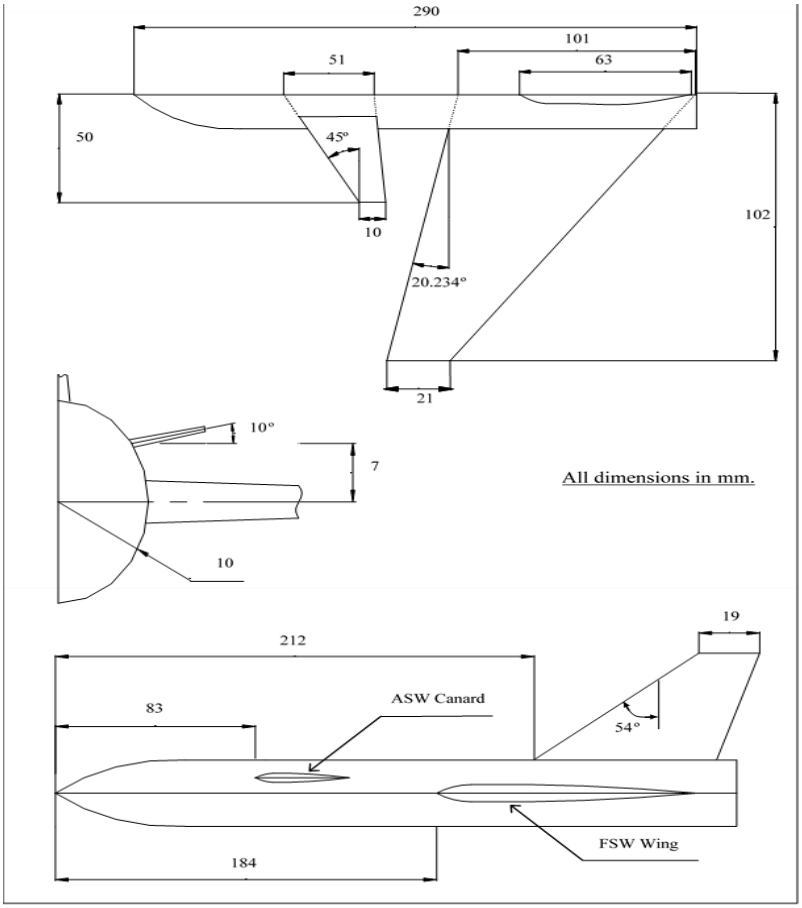

Fig. (4) The Geometrical Details of the Model.

Novelty Journals

ISSN 2394-9678

International Journal of Novel Research in Electrical and Mechanical Engineering
Vol. 5, Issue 1, pp: (19-29), Month: September 2017 - August 2018, Available at: www.noveltyjournals.com

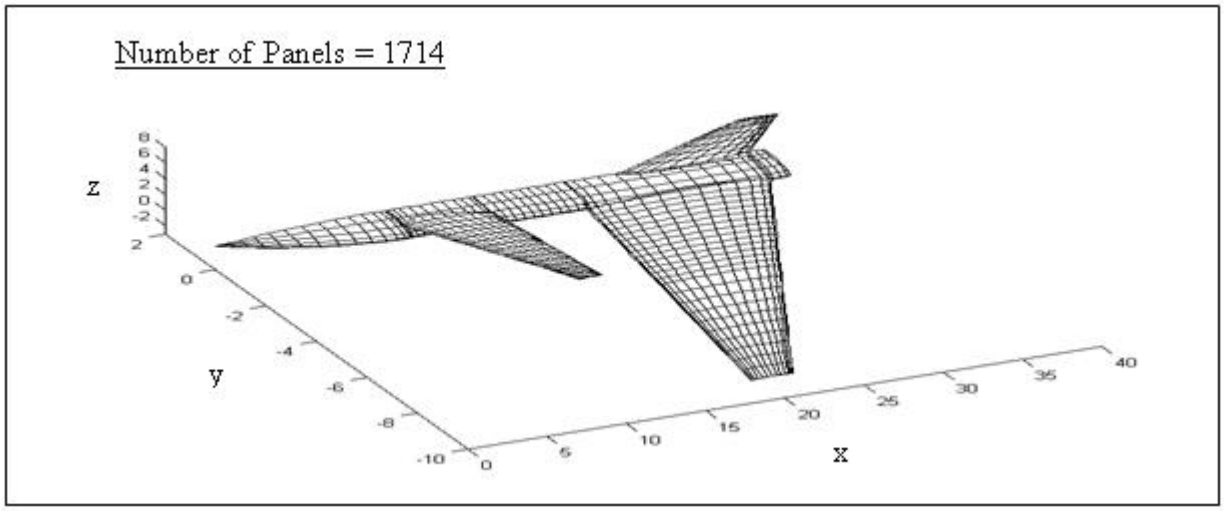

Fig. (5) Details of the Numerical Grid

V. NUMERICAL RESULTS

The aerodynamic characteristics of the FSW model were calculated and a qualitative comparison with the original model of Mann and Mercer (1986) was made, quantitative comparison could not be done due to the geometrical differences between the two models.

Fig. (6) shows the lift coefficient versus the angle of attack at subsonic flow condition (M_∞ = 0.6). It is seen that the difference between the numerical results and the experimental data is large. This is due to the body shape, dynamic dissimilarity, the assumption of the fixed wake geometry, and the compressibility effects. In general the behavior of the numerical solution is similar to the experimental data and the FSW-body-canard aerodynamic interference has been simulated accurately. The increment in the lift curve slope recorded in configuration (2) (canard on) is due to the additional lift produced by the canard.

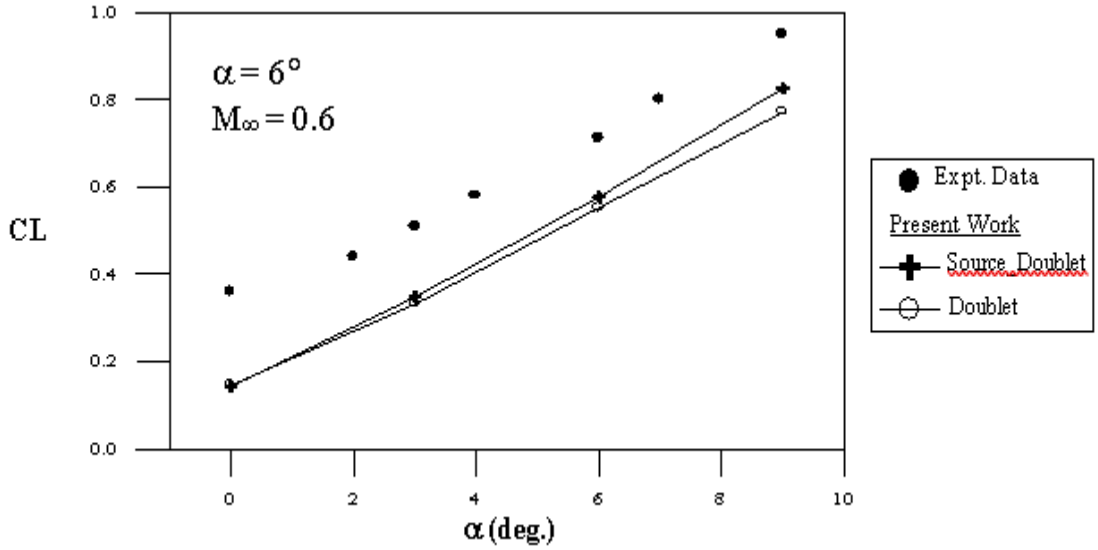

Fig. (6) Variation of the Calculated Lift Coefficient with Incidence. Configuration (2): Canard On

FSW span loading is shown in Fig. (7). The canard has changed the flow pattern over the FSW wing to a more balanced one. The heavily loaded root due to the FSW inboard flow and the body upwash has been relived by the canard downwash, while the FSW tips contribution to the lift has increased.

Novelty Journals

ISSN 2394-9678

International Journal of Novel Research in Electrical and Mechanical Engineering
Vol. 5, Issue 1, pp: (19-29), Month: September 2017 - August 2018, Available at: www.noveltyjournals.com

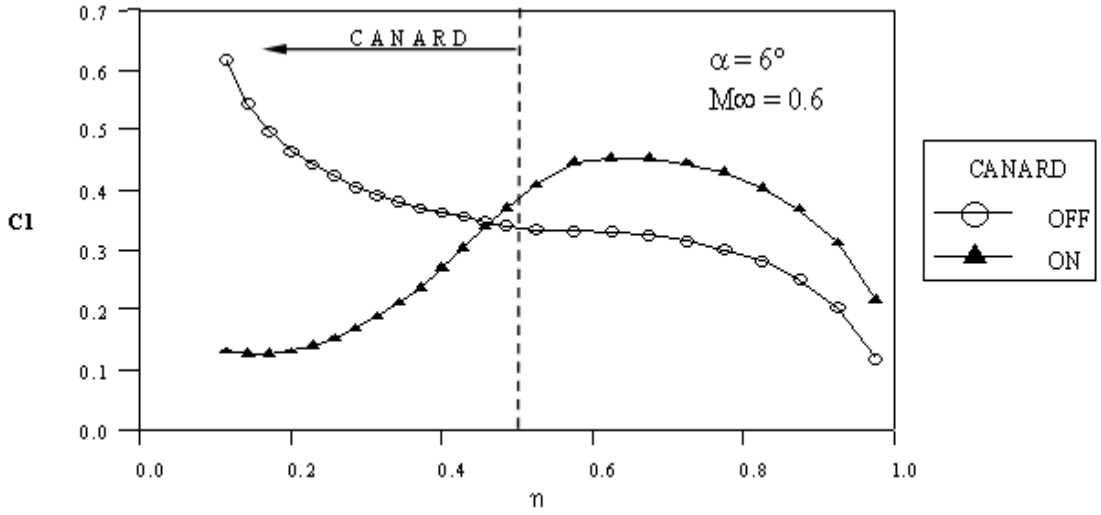

Fig. (7) Calculated Span Loading over the FSW

The pressure distribution over the main wing at different stations is shown in Fig. (8). It is seen that the installation of the canard causes a reduction in the pressure coefficients at the region covered by the canard downwash (up to $\eta = 0.5$), this is due to the reduced local angle of attack at that region. This reduction of the pressure (lower velocity) at the suction side of the wing will delay the separation at the root to a higher angle of attack. At ($\eta > 0.5$) the maximum pressure with the canard on exceeded that without canard. This is due to the canard upwash, which increase the local angle of attack at that part of the wing. This effect continues to the wing tips.

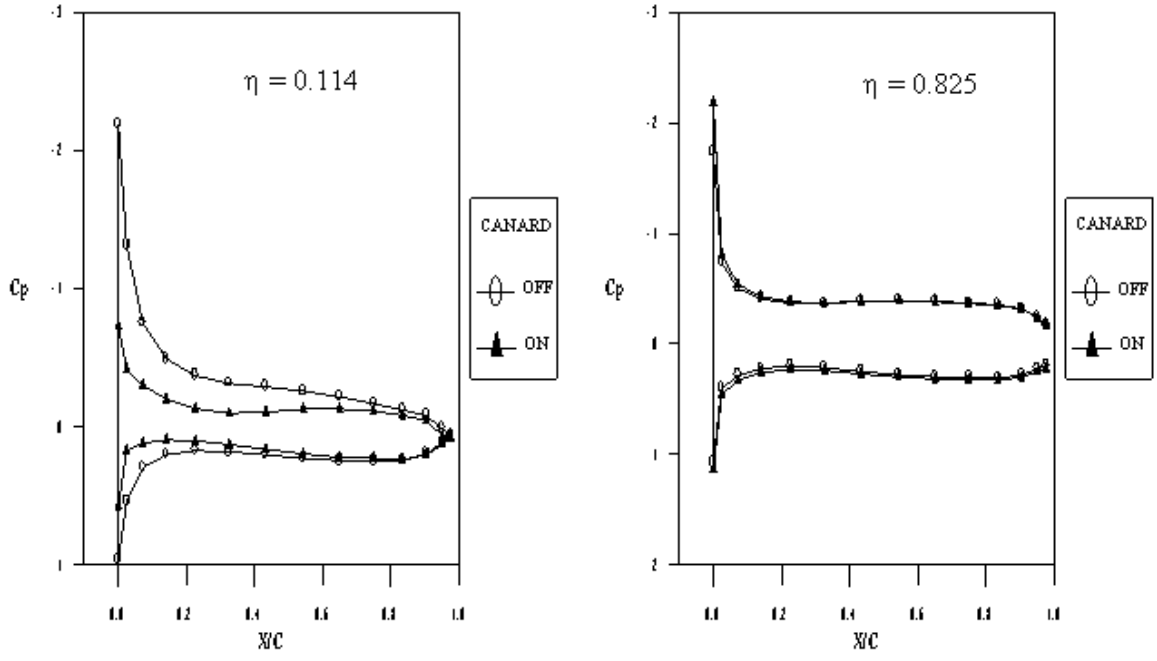

Fig. (8) Calculated Pressure Distribution over the FSW.

$\alpha = 6°$, $M_\infty = 0.6$

The pressure distribution along the body is shown in Fig. (9). The canard and wing interference on the body becomes stronger as the survey line becomes closer to the canard and wing positions. At ($\theta = 162°$) the wing-body-tail interference is clear, as there are two peaks (X/L = 0.65) corresponding to the wing and (X/L = 0.8) due to the tail. The wing effect is larger than the tail due to the airfoil section and incidence.

Novelty Journals

ISSN 2394-9678

International Journal of Novel Research in Electrical and Mechanical Engineering
Vol. 5, Issue 1, pp: (19-29), Month: September 2017 - August 2018, Available at: www.noveltyjournals.com

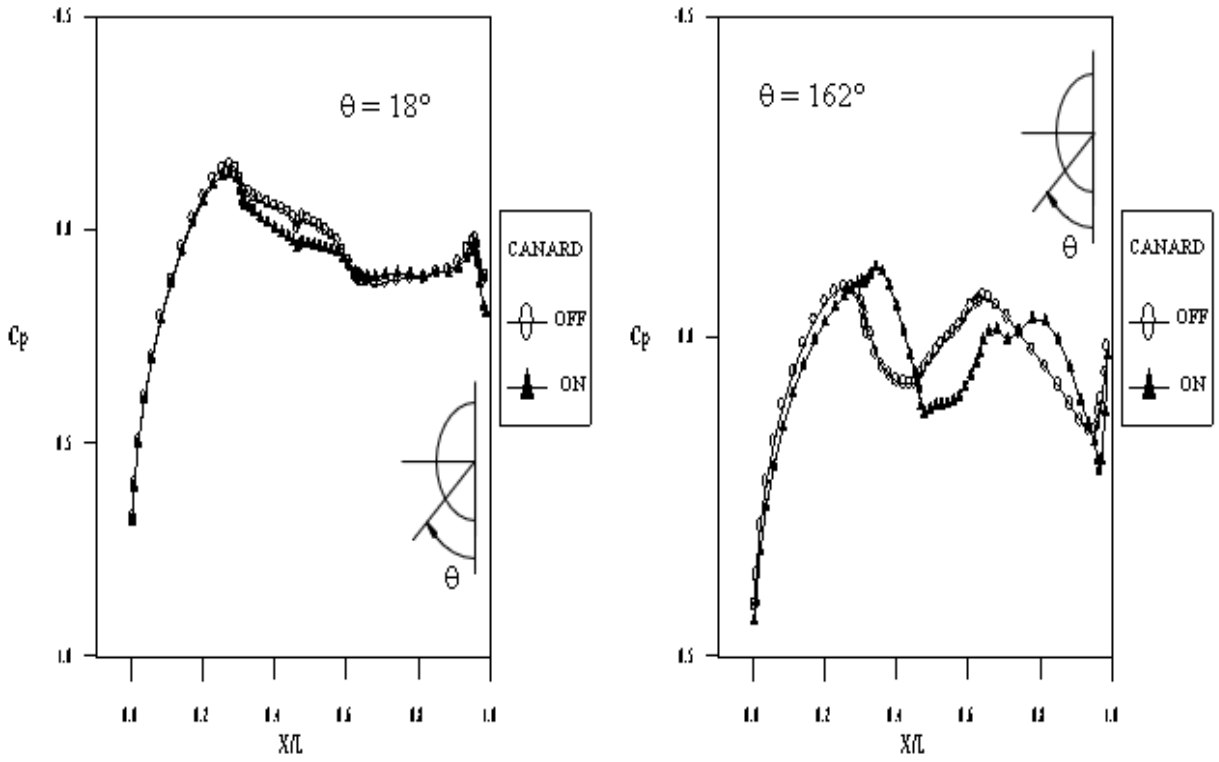

Fig. (9) Calculated Pressure Distribution along the Body

Fig. (10) shows the variation of the pitching moment coefficient about the apex of the body based on the mean aerodynamic chord of the wing. Due to the canard interference on the wing the pitching moment is reduced as compared to the canard off configuration. The lift and pitching moment curve slopes variation with the free stream Mach number are shown in Figs. (11) and (12) respectively. The lift curve slope with canard is higher than that without canard this is due to the additive lifting area provided by the canard. The pitching moment curve slope with canard is less than that without canard as the aerodynamic center has shifted toward the body apex.

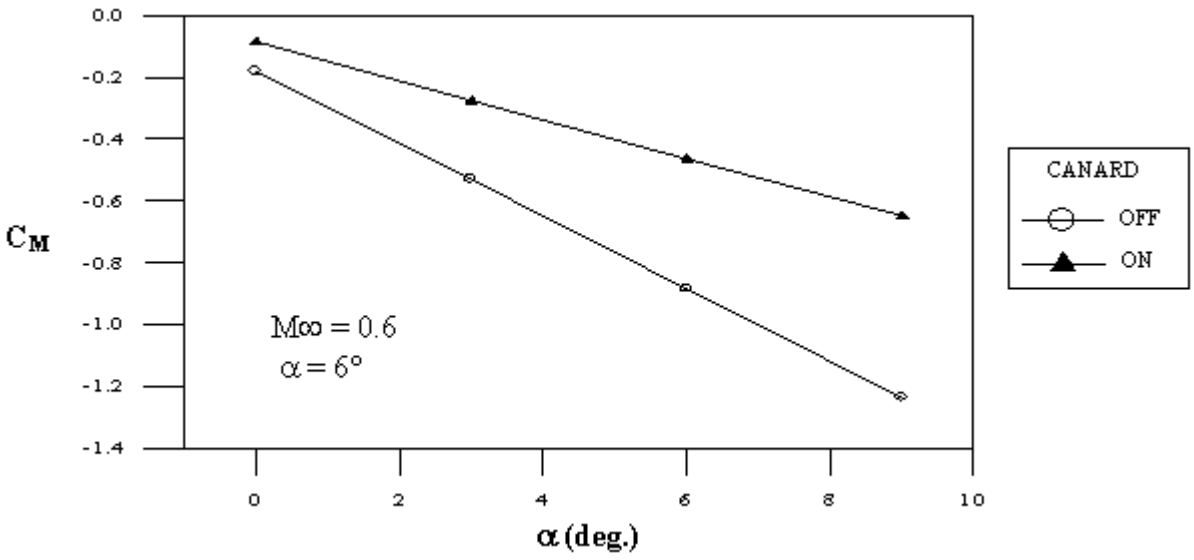

Fig. (10) Calculated Pitching Moment Coefficient versus Incidence

Novelty Journals

ISSN 2394-9678

International Journal of Novel Research in Electrical and Mechanical Engineering
Vol. 5, Issue 1, pp: (19-29), Month: September 2017 - August 2018, Available at: www.noveltyjournals.com

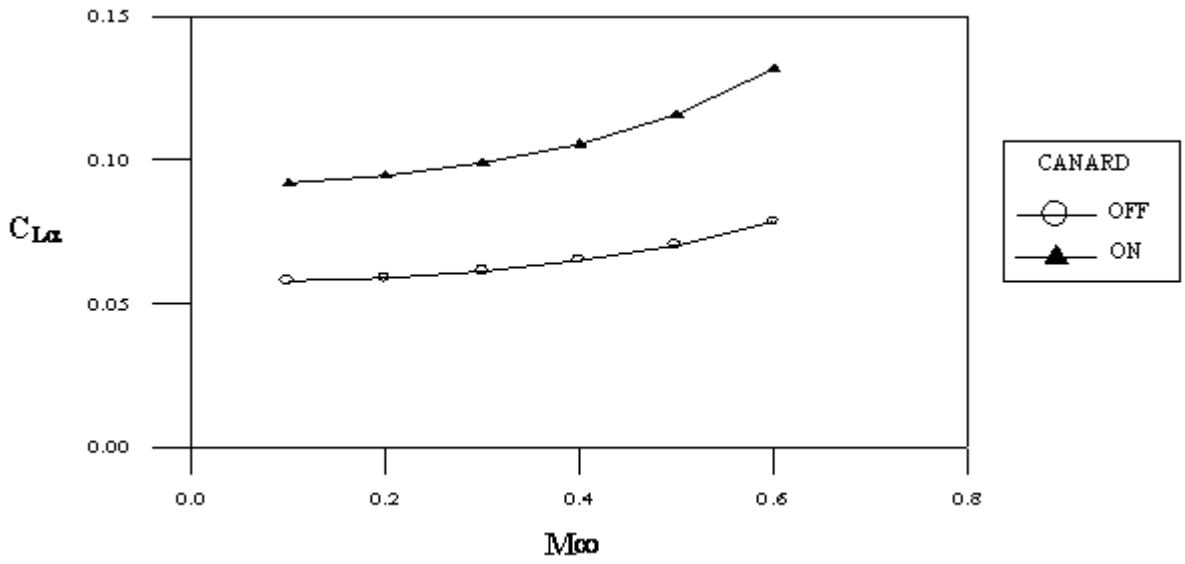

Fig. (11) Calculated Lift Coefficient versus Incidence

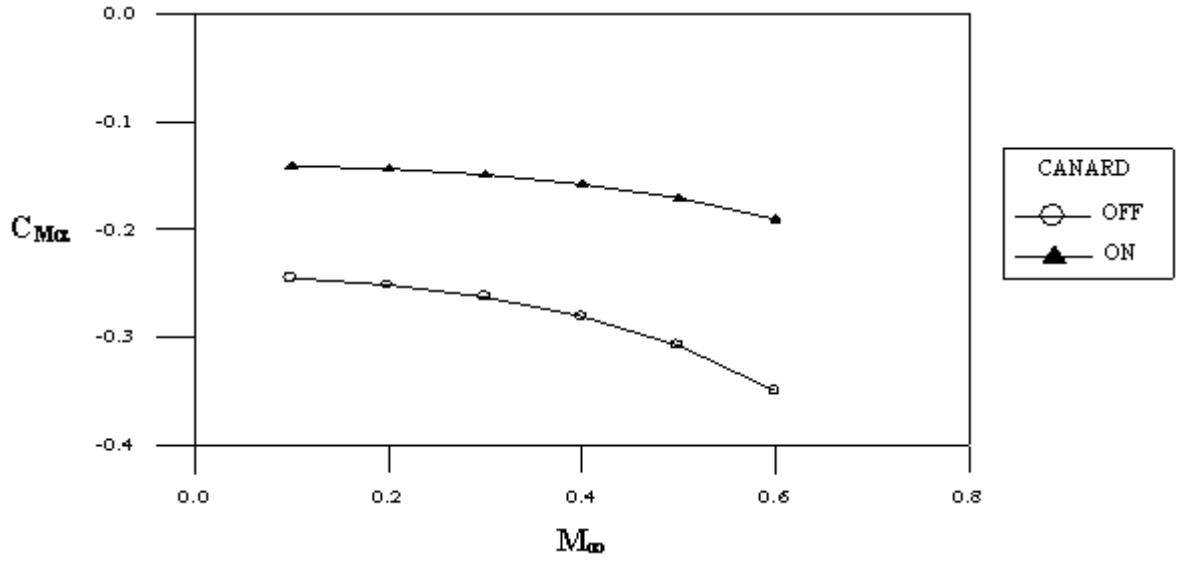

Fig. (12) Pitching Moment Coefficient Curve Slope with Mach Number

VI. CONCLUSIONS

The main conclusion obtained from the present work is that the low order panel method is capable of predicting the aerodynamic characteristics for the complex three-dimensional configurations in high subsonic and transonic speeds with good accuracy.

REFERENCES

[1] Arnott A. D., and Berstein L., (2000), Aerodynamic Interaction at the Junction Between a Forward Swept Wing and Plate, Aeronautical Journal, Vol. 104, No. 1023.

[2] Bandyopadhyay G., (1989), Low-Speed Aerodynamics of Canard Configurations, Aeronautical Journal, January.

[3] Edwin J. Saltzman, and John W. Hicks, (1994), In Flight Lift-Drag Characteristics for a Forward-Swept Wing Aircraft (and Comparison with Contemporary Aircraft, NASA TP-3414, December.

[4] John S. Letcher, (1989), Convergence of Lift and Drag Predictions by A Morino Panel Method (VSAERO), AIAA Journal, Vol. 27, No.8, August.

[5] John W. Hicks, and Thomas Huckabone, (1989), Preliminary Flight-Determined Subsonic Lift and Drag Characteristics of the X-29A Forward-Swept-Wing Airplane, NASA TM-100409, August.

[6] Michael J. Mann, and Charles E. Mercer, (1986), A Forward-Swept-Wing Fighter Configuration Designed by Transonic Computational Method, Journal of Aircraft, Vol. 23, No. 6, June.

[7] Morino L., Chen L. T., and Emil O. Suciu, (1975), Steady and Oscillatory Subsonic and Supersonic Aerodynamics around Complex Configuration, AIAA Journal, Vol. 13, No. 3.

[8] Rae H.W., and Pope A., (1984), Low Speed Wind Testing, John Wiley and Sons Inc.

[9] Singh N., Aikat S., and Basu B. C., (1989), Incompressible Potential Flow about Complete Aircraft Configurations, Aeronautical Journal, November.